PCCP

Accepted Manuscript

ROYAL SOCIETY OF CHEMISTRY

www.rsc.org/pccp

Physical Chemistry Chemical Physics

RSCPublishing

ARTICLE

Ultrathin undoped tetrahedral amorphous carbon films: Thickness dependence of the electronic structure and implications to electrochemical behaviour

Vera S. Protopopova*[1], Niklas Wester[1], Miguel A. Caro[2,3], Pavel G. Gabdullin[4], Tommi Palomäki[2], Tomi Laurila[2] and Jari Koskinen[1]

Cite this: DOI: 10.1039/x0xx00000x

Received 00th January 2014,
Accepted 00th January 2014

DOI: 10.1039/x0xx00000x

www.rsc.org/

In this paper we show that the electronic properties of ultrathin tetrahedral amorphous carbon (ta-C) films are heavily dependent on their thickness. By using scanning tunnelling spectroscopy, Raman spectroscopy, and conductive atomic force microscopy, it was found that a decrease of ta-C thickness from 30 to 7 nm leads to (i) a narrowing of the band gap; (ii) appearance of shallower monoenergetic traps as well as the increase of their concentration; (iii) the increase of the equilibrium concentration of free charge carriers and their mobility; which were caused by (iv) the increase in the sp^2 fraction. However, beyond a certain ta-C thickness (7 nm) the electronic properties of the studied samples start to deteriorate, which is highly likely related to titanium oxide formation at the Ti/ta-C interface. The same tendency is observed for the sample with beforehand air-formed native titanium oxide at the interface. With respect to the last point, it is suggested that the ta-C layer has not uniform coverage if its thickness is small enough (less than 7 nm). The experimental results were rationalized by detailed atomistic simulations. By using the so-called "Tauc plot" we introduce the possibility of the coexistence of bulk and surface band gaps originating from the large increase in sp^2 bonded carbon atoms in the surface region compared to that in the bulk ta-C. The results from the simulations were found to be consistent with the experimental measurements. The previously stated variation in the electronic properties of the layers as a function of their thickness was also exhibited in the electrochemical properties of the samples. It appears that the thinner ta-C layers had more facile electron transfer kinetics as determined with a ferrocenemethanole (FcMeOH) outer sphere redox system. However, if the ta-C layer thickness were reduced too much, the films were not stable anymore.

1. Introduction

Accurate detection of biomolecules is a challenging issue in modern medical research because it may help in revealing the mechanisms of many biochemical processes that are not understood completely yet. For instance, abnormal concentrations of the neurotransmitter dopamine are associated with several neurological disorders: *e.g.,* Parkinson's disease, schizophrenia, and Huntington's disease [1]. In the case of electrochemically active molecules such as dopamine, which electrochemical oxidation leads to the release of two protons and two electrons [2], they can be feasibly detected by means of special electrodes and cyclic voltammetry [3, 4]. Requirements of the electrode material include sensitivity, selectivity, long-term stability, biocompatibility, and ability to detect the released electron. From an electrochemistry point of view [5–7], band structure, distribution and concentration of vacant and occupied states, and free charge carrier concentration play a crucial role in electron transfer reactions taking place at the electrode–solution interface. Ideally, by knowing the molecular orbital structure of the detected biomolecule and the electronic structure of the electrode material, it is possible to predict or simulate the process of electron transport between the electrode and analyte [8], as well as to design the best electronic structure of the electrode material for the detection of a certain biomolecule.

Carbon-based electrode materials are widely used and intensively studied for biosensor applications [3, 9–19]. One such material is boron-doped diamond (BDD) [12–16] because of its excellent electrochemical properties such as wide water window, small background current, uniform surface, and biocompatibility. The main limitation factors of BDD electrode usage are the high deposition temperature required, which leads to incompatibility with integrated circuit processing, and limited range of substrates. An alternative prospective material is nitrogen-doped diamond-like carbon (N-DLC) [16–19],

which has the electrochemical properties that are almost as good as those of BDD [16, 18]. The benefit of using N-DLC is the possibility to deposit it under room temperature: for instance, by filtered cathodic vacuum arc (FCVA) deposition technique [20]. Nitrogen doping is needed for improving film electrical conductivity due to a higher amount of sp^2, when such an electrode is used for sensor applications [16–19]. In addition, nitrogen incorporation leads to obtaining of narrower band gap and decrease of internal stress and hardness in comparison to undoped DLC with the same thickness [21, 22]. However, N-DLC is not an ideal electrode material due to its limited electrical conductivity, high internal stress, and significant amount of pinholes, which typically does not permit the use of N-DLC films thinner than 100 nm [17]. Typical utilized thicknesses are in the range from 60–70 nm [23] to 1.5 μm [19].

Another way of increasing of sp^2 fraction without the pinhole number raise is to use ultrathin layers of undoped DLC. It should be mentioned that undoped hydrogen-free DLC is called tetrahedral amorphous carbon (ta-C). On the one hand, avoidance of nitrogen incorporation allows for a reduce number of pinholes. On the other hand, thickness decrease leads to increase of sp^2 fraction in ta-C thin films [24–26]. Only samples that were thicker than 60–70 nm maintain properties of bulk ta-C (Young's modulus, density, sp^3 fraction) [25, 26]. In addition, it was determined that there is a critical thickness for the ta-C layer (around 8–10 nm) that is needed for the stabilization of the sp^3 matrix structure [24]. The electronic properties of DLC layers have been studied relatively widely, including band gap determination with different methods [22, 27–30], investigations of the conduction mechanism [31–33], photoconductivity [34], and field emission properties [35].

The aim of this work is to study the electronic properties of ultrathin undoped ta-C thin films as a function of thickness and the possible implications for their electrochemical behaviour. Samples consisted of ta-C layers of different thickness deposited on top of highly-conductive p-type silicon with a 20-nm Ti interlayer. The band gap was measured by means of scanning tunnelling spectroscopy [27–30]. Raman spectroscopy was utilized for indirect indication of the sp^2/sp^3 ratio change by *I(D)/I(G)* ratio observation and shift of the G peak position, which also correlates with the band gap value [26, 36–38]. The conduction mechanism through the samples was analyzed in terms of space-charge-limited (SCL) currents theory [39] and was investigated by means of current–voltage curves obtained from atomic force microscopy operated in contact mode [32, 33]. Those measurements allowed for the study of electron transfer through the amorphous dielectric in order to specify the band gap structure of the samples, *i.e.* to find energy of traps or localized states, their concentration [40, 41]. In addition, electron transfer at the electrode–solution interface was probed by utilizing the redox molecule ferrocenemethanol (FcMeOH) by means of cyclic voltammetry [42]. Finally, to support the experimental work and rationalize the results, computational simulations using a combination of different levels of theory within the density functional theory framework [43, 44] were carried out.

It should be mentioned, that some preliminary experimental [11, 45, 46] and computational [49, 53] results have been obtained by our group in that field. We started [11, 45] from testing of electrochemical properties (water window, electron transfer at the electrode-solution interface with FcMeOH, sensitivity towards dopamine) of one kind of layered structure based on ta-C (VTT technical research centre of Finland). Then we compared one of those coating with new one [46], which demonstrated faster electrode kinetics and two orders of magnitude less detection limit to dopamine. Here, we continue that study focusing on new type of electrode structure.

2. Experimental details

2.1 Sample fabrication

The ta-C thin films were deposited on top of silicon with a 20 nm Ti underlying layer. The thickness of ta-C was varied in the range of 2–30 nm. Pieces of highly conductive (0.001–0.002 Ω cm) p-type boron-doped (100) silicon wafers with beforehand-deposited aluminium contact pad were utilized as substrates. Before the deposition, Si wafers were cleaned by standard RCA-cleaning procedure and acetone ultrasonication. Ti and Al layers were deposited by means of direct-current magnetron sputtering (DC-MS); whereas ta-C layers were obtained *via* filtered cathodic vacuum arc (FCVA) deposition.

All used deposition setups were installed in a 125-l cylindrical stainless steel deposition chamber. The chamber vacuum was pumped down by a dry-scroll vacuum pump (Edwards XDS10) and by a cryo pump Cryo-Torr (Helix Technology corporation). In order to get the low vacuum level needed for DC-MS, a high-vacuum throttle valve was used. Two magnetron sputtering systems were equipped with two circular water-cooled magnetron sputtering sources with 2-inch Ti and 4-inch Al targets (Kurt J. Lesker Company), respectively, and by a DC generator (DCO2 BP) as well. The shutters were utilized for sputtering time control. The crystal oscillator film-thickness monitor (SQM 242) was used for thickness control during the process. Pre-sputtering of 120 s was carried out for the target surface cleaning. Titanium layers were deposited under the following deposition conditions: discharge power was fixed at 100 W, total pressure was 0.67 Pa, Ar gas flow rate was 28 sccm, and deposition time was 350 s. Deposition rate was 0.57 Å/s when the distance between the substrate holder and the target was about 20 cm. The FCVA system was equipped with a 60° bent magnetic filter for macroparticle contamination reduction. Two 99.997 % graphite rods (Goodfellow) of diameter 6.35 mm were used as the carbon cathodes, which were surrounded by a cylindrical anode. The arc current pulses had the amplitude of 0.7 kA and 0.6 ms pulse width. Each pulse was triggered at 1 Hz frequency. The 2.6 mF capacitor bank was charged to 400 V. The total pressure during the deposition process was no more than $1.3 \cdot 10^{-4}$ Pa. The deposition rate was 0.2 Å/pulse in the

case when the distance between the substrate holder and the filter border was about 20 cm. Samples were placed in the not-heated, grounded rotating holder (rotational velocity used was 20 rpm).

Besides desired bilayer structures, sets of single metal and single ta-C layers with various thickness values were fabricated on Si to determine the deposition rates. The real thickness values of such single layers were measured by means of profilometer Dektac XT with 6 Å step height repeatability. Calibration curves of the single layer thickness *vs* the deposition time for the DC-MS process or pulse numbers for FCVA were determined (not presented here) and were used for the previously mentioned deposition rate value determination.

2.2. Physical methods of sample characterization

Scanning probe multimicroscopes Ntegra Aura (NT-MDT Company) and SMM 2000 Vac (Proton-MIET) were utilized for scanning tunnelling microscopy (STM) and spectroscopy (STS) in ambient air and under high vacuum (10^{-5} Pa) conditions, respectively. With the use of STS, investigation of the density of states (DOS) near the Fermi level was carried out by measuring the differential conductivity dI_{TUN}/dU_{BIAS} of the tunnel current depending on voltage applied to the sample surface. Registration of the I_{TUN}–U_{BIAS} characteristics of the tunnelling current was done for different randomly chosen surface areas of studied samples by the interrupted-feedback technique. At least ten measurements were obtained for each point to reduce the possible error due to tip–sample spacing variation. All measurements were carried out under such conditions, when I_{TUN}–U_{BIAS} characteristics did not depend on tip voltage, in order to prevent the influence of tunnel contact. It means that resistance of tip–sample spacing was negligibly small in comparison to the effective resistance of sample and obtained I_{TUN}–U_{BIAS} characteristics related to the DOS of the studied sample. The measurement conditions, such as tip current and tip voltage, were 0.2 nA and 0.5 V and 1 nA and 1 V for the Ntegra Aura and SMM 2000 Vac microscopes, respectively.

Visible Raman spectroscopy (WITec alpha 300 spectrometer) was used as an effective way to investigate the bonding structure of ta-C films. For all kinds of amorphous and nanocrystalline carbon films, Raman spectrum typically shows a G-band peak centred around 1550 cm^{-1} and a D-band peak centred at 1360 cm^{-1} [26, 36–38, 47]. Nevertheless, it was demonstrated that both peaks are caused by sp^2 fraction, while the intensity ratio of D-band to G-band *I(D)/I(G)* and shift of the G peak are correlated to the sp^3/sp^2 ratio, the band gap value, and film density [26]. The following spectra-acquisition parameters were used: laser wavelength was 532 nm, exposure time was 0.5 s, number of accumulation is ten, and spectrum wave number was in the range of 450 to 3900 cm^{-1}. All obtained spectra were processed by an averaging of 50 spectra and a background subtraction.

Besides performing STM and STS measurements, scanning probe multimicroscope Ntegra Aura (NT-MDT Company) was used for contact atomic force microscopy (AFM) and spreading resistance microscopy (SRM or conductive-AFM). The measurements were carried out in 'scanning by sample' mode with the use of universal measuring head equipped with the special probe holder designed for current measurements. Diamond-coated conductive probes (DCP10) with a typical curvature radius of 100 nm and nominal force constant of 11.5 N/m were used. Conductive-AFM was performed in single-pass mode, which permitted the acquisition of simultaneously topography maps, roughness data, current maps, current distribution, and the average current J_{SR} flowing through the studied sample area under the voltage U_{SR} applied to the probe, which value was 0.5 V in most cases. Bitmap images were processed using the free software Gwiddion 2.34.

In addition, current–voltage spectroscopy, which allows the acquisition of J_{SR}–U_{SR} characteristics in point, was used for investigations of the conduction mechanism in terms of space-charge-limited (SCL) currents theory. The presence of defect states or traps in the band gap can be found as well. During the measurements, the range of the applied voltage values varied from sample to sample and was limited by the maximum measured current of ±25 nA. All obtained J_{SR}–U_{SR} characteristics were the average of ten measurements in different points.

2.3. Cyclic voltammetry

The electrochemical properties of the fabricated electrodes were measured with cyclic voltammetry. A Gamry Reference 600 Potentiostat/Galvanostat/ZRA and a three-electrode configuration measurement cell were used. The reference electrode was a Ag/AgCl skinny reference electrode (Sarissa Biomedical ltd., Coventry, UK) and the counter electrode was glassy carbon. The backside of the samples was contacted to a copper plate. The copper plate and sample were covered with Teflon tape, with a pre-made hole with a 6 mm diameter. The tape covered the sample and copper plate in such a way that the solution could make contact with the sample surface only through the hole. Water windows were measured both in 0.15 M sulfuric acid and phosphate buffered saline (PBS) solution at sweep rates of 50 and 400 mV/s. The pH values of the PBS solution and sulfuric acid were 7.4 and 0.90, respectively.

The outer-sphere redox system Ferrocenemethanol (FcMeOH) was used to define the electron transfer rate of the electrodes. The 1 mM FcMeOH solution was prepared by using Ferrocenemethanol (Sigma-Aldrich, St. Louis, USA) in 100 mL of 0.15 M sulfuric acid (Merck kGaA, Darmstadt, Germany). FcMeOH measurements were carried out at sweep rates of 50 and 400 mV/s for each electrode. Prior to measurements, the solutions were saturated with N_2 for 5 min and during measurement the cell was kept at N_2 atmosphere. All measurements were carried out at room temperature and the FcMeOH solutions were prepared on the day of the measurement to prevent its oxidation.

2.4. Band gap prediction by density functional theory

The Tauc gap is determined from the onset of linear absorption, obtained as the intersection of a linear fit to the absorption curve in the region where it behaves linearly [48]. From the computational point of view, the absorption coefficient α can be obtained as a function of photon energy from the product of the square of the dipole matrix element for interband absorption M and the joint density of states (JDOS) [49, 50]:

$$\alpha(\hbar\omega) = M^2(\hbar\omega)\int_{-\infty}^{\infty} dE\rho_{VB}(E)\rho_{CB}(E+\hbar\omega) \quad (1)$$

where $\hbar\omega$ is the energy of the absorbed photon, $\rho_{VB}(E)$ and $\rho_{CB}(E)$ are the density of states at energy E for the valence and conduction bands, respectively, and the result of the integral is what is known as the JDOS. The evolution of the square root of the JDOS as a function of photon energy is the quantity used for the Tauc gap determination [50]. The computational samples used in this study were generated following the guidelines given in our recent paper [51] using the PBE [52] functional within the frame of density functional theory (DFT) [43, 44]. The samples chosen for the present study are the bulk structures from Ref. [51] with sp^3 content above 50 %. Given the inherent issues of standard DFT with respect to band gap determination [53], we used the HSE hybrid functional [54] for accurate prediction of the energetic positions of electronic states for one of the samples (density 3.03 g/cm^3 and sp^3 fraction of 72.4 %). The calculation scheme is described in detail elsewhere [55]. All the DFT simulations were carried out with the VASP package [56] using the PAW method [57, 58]. Given the high computational cost of hybrid functional calculations, only one sp^3 fraction value could be explored. Future work shall extend the present computational band gap calculations to a wider range of sp^3 values.

3. Results and discussion

3.1 Experimental determination of band gap and bonding structure

Figure 1a shows dependencies of tunnelling current I_{TUN} and differential conductivity dI_{TUN}/dU_{BIAS} on sample voltage obtained from the sample surface with a 30-nm thick ta-C layer measured in ambient air (dot line) and under vacuum conditions (solid line). The DOS of the studied sample is proportional to the differential conductivity [59]. However, negligible importance of several factors, such as the effect of electric fields on the surface DOS, the influence of the tip DOS, and the tunnelling transmission probability, is suspected. It is to be noted that both dependencies obtained in ambient air and under vacuum conditions agree within uncertainties. (i) Firstly, valence and conduction band edges have significant tails caused by amorphous structure of samples. For example, in the case of amorphous silicon [60], the valence tail is due to structural disorder, while the conduction tail is sensitive to temperature and originates from thermal disorder (in our case, measurements were carried out at room temperature). This is the reason why the tails are not symmetrical. (ii) Secondly, the fine structure related to local maxima and minima reproduce each other quite well. Because of unsharp band gap edges and extensive tails, it was difficult to find the actual band gap value. Therefore, mobility edges were found as the energy levels separating extended (non-localized) states of valence and conduction bands from localized states of exponential tails. We will discuss further the mobility gap value.

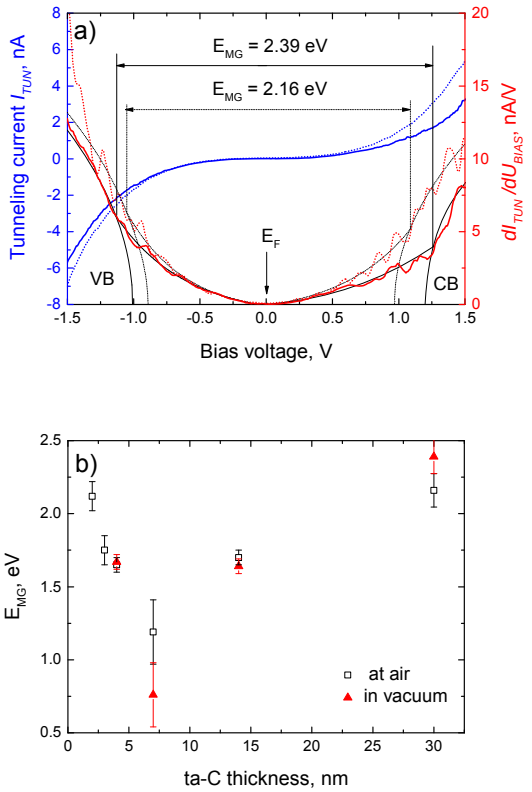

Figure 1. (a) I_{TUN}–U_{BIAS} characteristics (left vertical axis) and differential conductivity dI_{TUN}/dU_{BIAS} (right vertical axis) obtained at ambient air (dot line) and vacuum (solid line) conditions for the sample with 30 nm top ta-C layer. (b) Dependence of the mobility gap value on ta-C thickness.

The dependence of the mobility gap values on ta-C thickness is presented in Figure 1b. This plot has a clear minimum around 7 nm thickness of the ta-C layer. The smallest value of mobility gap is 1.19±0.2 or 0.76±0.2 eV according STM measurements carried out at ambient air or vacuum conditions, respectively. The band gap value reduces from 2.39±0.12 or 2.16±0.12 eV (air, vacuum) to the minimum value with a decrease in thickness from 30 to 7 nm, which correlates well to results published [24–26] and can be associated with a greater amount of sp^2 fraction [22, 24, 61]. The gap value of 2.39±0.12 eV is also consistent with the results presented in the literature for the bulk ta-C [27, 28]. However, further decrease of ta-C thickness to 2 nm leads to the drastic increase of the gap value to 2.12±0.1 eV (air). An increase of the band gap value

with the decrease of the layer thickness is often observed for nanocrystalline thin films [62–64], due to the quantum confinement effect, when the grain size diminishes with the thickness decrease. In a contrast, in the case of amorphous layers, their thickness decrease [65–67] usually leads to the band gap narrowing. Moreover, the decrease of DLC layer thickness causes higher sp^3 fraction and wider band gap [24–26]. Therefore, another explanation should exist for the band gap broadening with ta-C thickness decrease from 7 to 2 nm. We suggested that the change of properties of Ti underlying layer can play a crucial role. For instance, titanium oxide layer formation at the Ti/ta-C interface can induce the observed behaviour. The latter change is expected to occur due to nonuniform coverage of ta-C layer. It should be mentioned that both the surface and bulk DOS contributed to the resulting I_{TUN}–U_{BIAS} spectra of tunnelling current. Contribution of each depends on tip height in a way that the bulk DOS is prevalent in the case of lower tip height, while the surface DOS dominates at larger tip height [68]. Therefore, it is assumed that STS results give an average representation of the overlying surface and bulk DOS. In the case of ultrathin ta-C layers, the DOS of the underlying layer, especially if it is an oxide layer with a wider value of band gap, can affect the resulting spectra.

In order to study the ta-C bonding structure, the samples were characterized by means of Raman spectroscopy. Raman spectra and results of their analysis are presented in Figures 2a and 2b. Samples containing 2- and 3-nm thick ta-C were too thin to get reasonable signal. Figure 2b indicates that the value of the *I(D)/I(G)* ratio increases monotonically with the ta-C thickness decrease. This behaviour is most likely to be connected with the observed trends in the magnitude of the band gap and the sp^3/sp^2 ratio [36–38] in such a way that when the *I(D)/I(G)* ratio decreases and there is a simultaneous shift in the G-peak wave number to lower values; the band gap and the sp^3/sp^2 ratio both increase. Those results correlate well with the data presented in [24–26], where the amount of the sp^2 fraction is reported to decrease as the film thickness increases for all ranges of ta-C thickness values used. However, STS measurements indicate that the band gap value for the sample with the 4-nm top ta-C layer is wider than for the sample with the 7-nm ta-C layer. This result is understood in terms of Raman results correlating with change of ta-C band gap values only and excluding the influence from the underlying layer because of the investigation of specific wavelengths distinctive to carbon bonds.

Thus, comparison of STS and Raman results indicates that the ta-C band gap decreases as thickness decreases. However, the titanium oxide layer starts forming in the Ti/ta-C interface when ta-C layer becomes thinner than 7 nm, which leads to appearance of wider band gap values. This can influence electron transfer properties of the whole multilayer structure during electrochemical measurements, which will be described later.

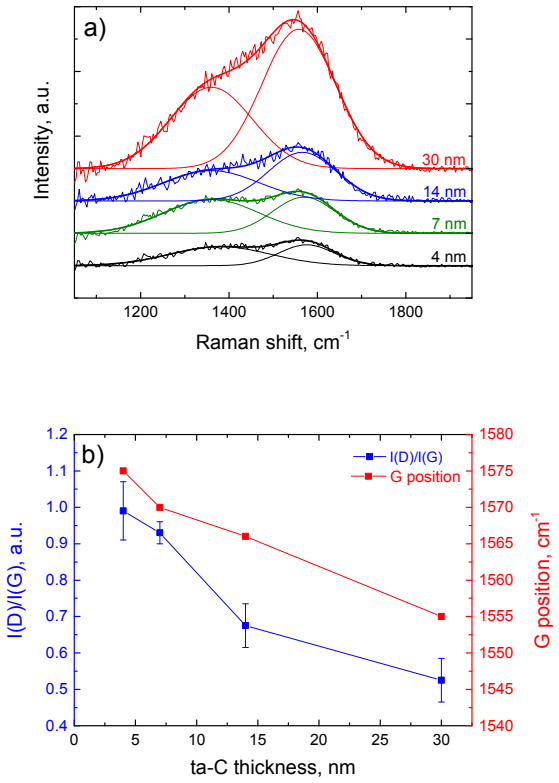

Figure 2. (a) Raman spectrum of ta-C with different thicknesses and (b) dependences of *I(D)/I(G)* ratio and G-band position on ta-C thickness found from analysis of (a).

3.2. Conductive AFM and space-charge-limited currents

In order to investigate the electron conduction mechanism throughout the electrode structure, conductive AFM and current-voltage spectroscopy were carried out in contact (spreading resistance) mode. The results from conductive-AFM are presented in Figure 3.

The analysis of the topography maps (Figures 3a–f) shows that all the samples have approximately the same roughness of 1 nm and that the surface features are also of similar diameter (approximately 150 nm). Preliminarily results obtained by means of AFM shows that the topography of top ta-C layer repeats the topography (roughness and the surface features size) of the underneath Ti layer. Thus, it is likely that the uniform top ta-C layer covers the rough Ti underneath layer almost conformally.

The analysis of the current maps (Figure 3a'–f') indicates an uneven distribution of the current J_{SR} flowing through the samples under the applied probe voltage U_{SR}. Round or oval local spots that are less conductive are surrounded by a more highly conductive net. The average diameter of such spots is around 150 nm, which agrees with the features size seen in the topography maps (Figures 3a–f). Comparison of topography and current maps confirms that the less conductive spots relate to hills from topography, while the highly conductive net coincides with the valleys. Such behaviour can be caused by

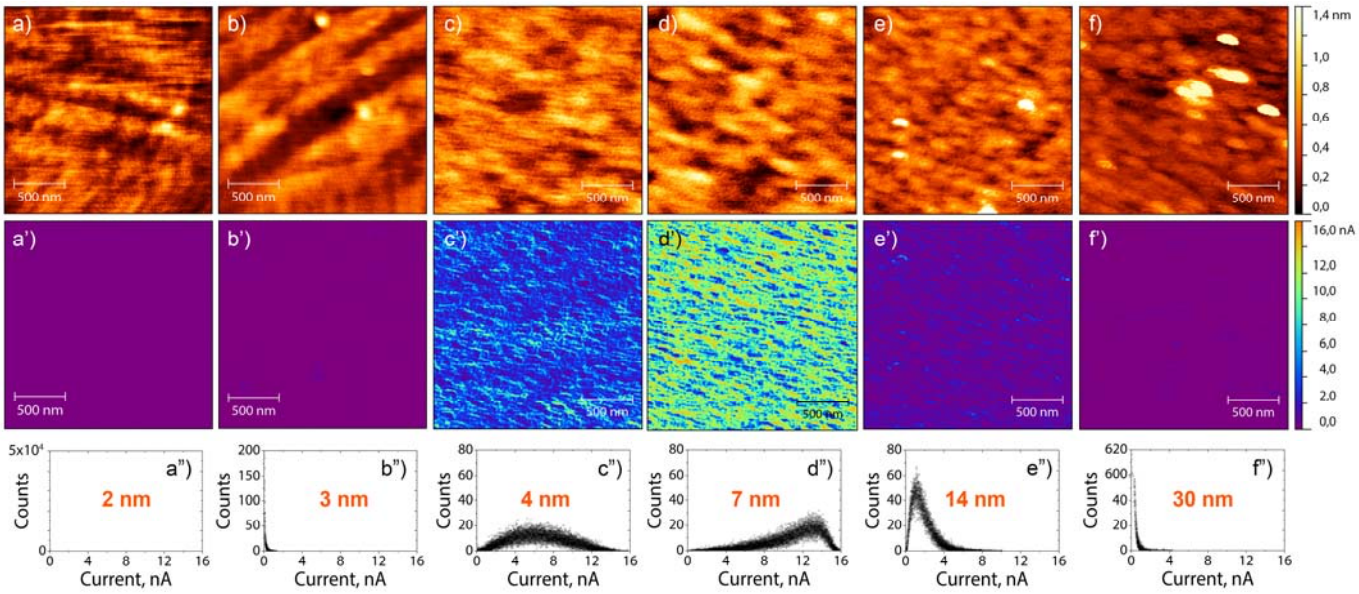

Figure 3. (a–f) Topography maps, (a'–f') maps of current J_{SR} and (a"–f") distribution of current J_{SR} for samples with different ta-C thicknesses (under 0.5 V).

different values of mechanical contact area of a real granular or rough surface (in cases of hills or valleys) as has been previously demonstrated [69].

Distributions of current J_{SR} presented in Figure 3a"–f" are used in order to obtain the dependence of the average current (as it correlates to the maximum current in the distribution) flowing through the sample on the ta-C thickness shown in Figure 4. A particular feature of this dependence (Figure 4) is the presence of the current extreme for the sample with 7-nm thick ta-C. The average current J_{SR} increases from 0.07 to 12.3 nA (measured under 0.5 V of applied voltage) and the specific resistance decreases from $4.02 \cdot 10^4$ to 200 Ω cm (Table 1) simultaneously with mobility gap reduction (Figure 1b) with a ta-C thickness decrease from 30 to 7 nm. Further ta-C thickness decrease to 2 nm leads to a rapid fall of the value of average current to 2.5 pA (Figure 4); specific resistance increases to $1.13 \cdot 10^6$ Ω cm (Table 1) at the same time as the mobility gap increase (Figure 1b). The values of specific resistance ρ were found from equation (2) for voltage between the probe with hemisphere shape and the collecting contact of radius r_C, where U_{SR} and J_{SR} is measured voltage and current. Contact radius r_C was calculated from Hertz elastic contact theory [69] for ball–ball contact and was found to be 7.5 nm.

$$U_{SR} = \frac{\rho J_{SR}}{2\pi r_C} \qquad (4)$$

In order to determine an explanation for why samples with thinner ta-C layers (2–4 nm) and samples with thicker ta-C (7–30 nm) have such different electrical behaviour, the electrical conduction mechanism through the samples must be further considered. The system under study included a metal (Ti deposited on Al contact pad), dielectric (ta-C), and semiconductor (nitrogen doped diamond coating of AFM probe). The substrate presence (Si) can be neglected from consideration as it does not participate in the current transport. Thus the only parameter that was changed was the ta-C layer thickness. However, titanium oxidation should be taken into account as we suggested above.

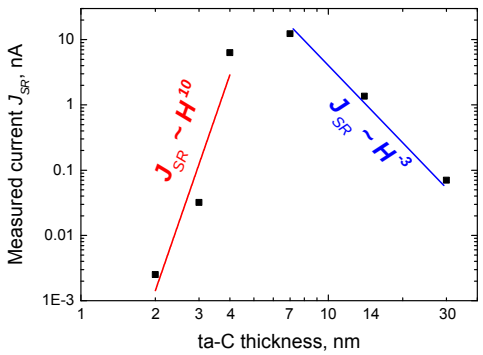

Figure 4. Dependences of the average current J_{SR} flowing through the sample on ta-C thickness at the probe voltage of 0.5 V.

The mechanism of electrical conduction in dielectric thin films can be described and investigated in terms of space-charge-limited (SCL) injected currents model [32, 39–41]. The studied current–voltage characteristics are plotted in log–log coordinates and presented in Figure 5, where linear regions relate to $J \sim U^N$ dependence (N values are marked near all linear regions). It should be noted that typically a current–voltage curve plotted in log–log coordinates contains at least three regions indicative of the different conduction mechanism; these are:

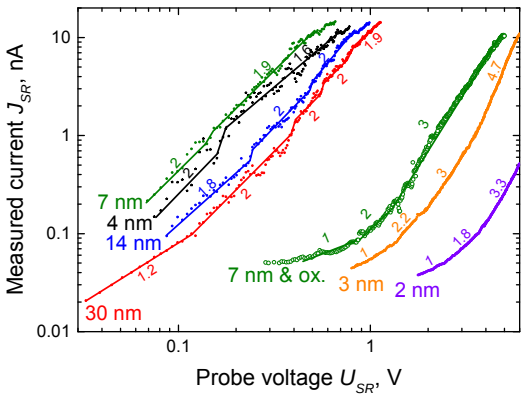

Figure 5. Current–voltage curves obtained from samples with different ta-C thicknesses plotted in log–log coordinates. (Sample '7 nm & ox' contains air-formed native titanium oxide at Ti/ta-C interface. See paragraph 3.3) The numbers placed along the lines of approximations represent the slopes at those locations.

1. Ohm's law region (equation 3), which is usually observed at low applied voltages. Unit slope (N=1) appears in log–log coordinates. If the applied voltage becomes bigger than a certain transition voltage U_{TR} (4), the linear dependence (N=1) changes to a quadratic law (N=2). Under voltages less than U_{TR}, the thermally generated carrier density (n_0) dominates over the injected carrier density; therefore, equation (4) can be used for n_0 estimation. In the case, when resistance (conductance) is known, carrier mobility μ can be found using equation (5).

In the case of samples with ta-C thickness in the range of 4–30 nm (Figure 5), U_{TR} values are very low. Ohm's law is not readily observed in the case of samples with 4, 7, and 14 nm ta-C thicknesses, therefore n_0 and mobility values (presented in Table 1) can be overestimated. For samples with the thinnest ta-C layers (2 and 3 nm), Ohm's law smoothly transitions to the first quadratic and then to a sharper law.

2. The first quadratic law is related to the presence of monoenergetic traps (single carriers) in the band gap. In this case, SCL current density is expressed by the Mott–Gurney law (6). The first quadratic region is followed by the sharp increase of measured current at the trap-filled limit voltage U_{TFL} (7) when all traps are occupied. Trap energy (trap depth from the edge of conduction band) can be found from equation (8). It should be noted that several (m) quadratic laws can be observed, which means that the first (m–1) quadratic regions correlate to presence of (m–1) levels of monoenergetic traps with different depth and the last quadratic law relates to Child's law (described below).

Current–voltage characteristics for samples with 4- and 7-nm thick ta-C layers (Figure 5) contain two quadratic regions; so one region relates to the presence of monoenergetic traps and space charge formation due to trapped electrons. In the case of samples with 14- and 30-nm ta-C layers, J_{SR}–U_{SR} contains three and four quadratic regions; thus, two and three single traps can be found. The presence of monoenergetic traps can be also confirmed by the dependence of the average current on ta-C thickness. According to equation (6), the measured current is inversely proportional to thickness cubed. As is illustrated in Figure 4, an inverse cubic dependence is observed for samples with ta-C thickness in the range of 7–30 nm, while the point for the sample with 4 nm ta-C layer is already out of this dependence.

3. The second quadratic law (or the last, in case of (m) quadratic laws) appears when all traps are filled and conduction becomes space-charge limited (Child's law), which limits the further injection of free carriers in the dielectric. Child's law is expressed as (9). In certain cases, when a region with $N \geq 3$ is found, it means that SCL currents are limited by exponentially distributed traps. Characteristic trap energy for exponentially distributed traps can be found from equation (10).

The current–voltage characteristics of samples with 2- and 3-nm ta-C layers (Figure 5) do not have signified or separated regions with different slopes. However, the largest linear regions correlate to N values of 3.3 and 4.7. In this case, the conduction mechanism is defined by exponentially distributed traps, which is also supported by the sharp fall of the average measured current with thickness decrease.

$$J_{Ohm} = en_0\mu\frac{U}{H}, \qquad (3)$$

Table 1. The results from analysis of current–voltage characteristics for samples with different ta-C thicknesses.

ta-C thickness, nm	ρ, Ω cm	U_{TR}, V	n_0, cm^{-1}	μ, cm^2/V s	U_{TFL}, V	θ	N_t, cm^{-1}	E_t, eV	Conduction mechanism
2	$1.13\cdot10^{6}$	2.6	$2.0\cdot10^{19}$	$2.8\cdot10^{-7}$	-	-	-	0.095	SCLC with exponentially distributed traps
3	$8.79\cdot10^{5}$	1.26	$7.1\cdot10^{18}$	$1.0\cdot10^{-5}$	-	-	-	0.059	SCLC with exponentially distributed traps
4	443	<0.075	$5.5\cdot10^{17}$	$2.5\cdot10^{-2}$	0.163	0.85	$2.7\cdot10^{18}$	0.037	SCLC with monoenergetic traps
7	200	<0.07	$1.7\cdot10^{17}$	0.18	0.143	0.88	$8.4\cdot10^{17}$	0.067	SCLC with monoenergetic traps
7 nm & ox	$3.22\cdot10^{4}$	0.86	$5.7\cdot10^{17}$	$3.4\cdot10^{-4}$	-	-	-	0.045	SCLC with exponentially distributed traps
14	$2.07\cdot10^{3}$	<0.087	$6.6\cdot10^{16}$	$4.6\cdot10^{-2}$	0.24 0.49	1 1	$3.3\cdot10^{17}$ $6.9\cdot10^{17}$	0.086 0.067	SCLC with monoenergetic traps
30	$4.02\cdot10^{4}$	0.117	$1.9\cdot10^{16}$	$8.1\cdot10^{-3}$	0.39 0.56 0.77	1 1 1	$1.2\cdot10^{17}$ $1.7\cdot10^{17}$ $2.3\cdot10^{17}$	0.112 0.103 0.096	SCLC with monoenergetic traps

$$U_{TR} = \frac{8}{9}\frac{en_0H^2}{\varepsilon\varepsilon_0\theta}, \quad (4)$$

$$\sigma_0 = n_0 \cdot e\mu, \quad (5)$$

$$J = \frac{9}{8}\varepsilon\varepsilon_0\theta\frac{U^2}{H^3}, \quad (6)$$

$$U_{TFL} = \frac{eN_tH^2}{2\varepsilon\varepsilon_0}, \quad (7)$$

$$E_t = kT\ln\frac{N_C}{\theta \cdot N_t}, \quad (8)$$

$$J_{Child} = \frac{9}{8}\varepsilon\varepsilon_0\theta\frac{U^2}{H^3}, \quad (9)$$

$$J = e\mu N_C\left(\frac{\varepsilon\varepsilon_0}{N_t}\right)^l\frac{U^{l+1}}{H^{2l+1}}, \quad (10)$$

where e is electron charge, n_0 is equilibrium concentration of thermally generated free charge carriers, μ is electron mobility, H is layer thickness, ε is relative permittivity, ε_0 is the permittivity of vacuum, θ is the trapping parameter showing the ratio of occupied and unoccupied traps, N_t is trap concentration, N_c is effective density of states in the conduction band (~ 10^{19} cm^{-1} at room temperature), and (l+1) is equal to N. According to equations (3–10) from SCL currents theory, the trap energy, and their concentration, the number of free charge carriers and their mobility are calculated and presented in Table 1.

The results from the analysis of measured current–voltage characteristics (Figure 5 and Table 1) indicate that (i) shallow traps exist in all cases; (ii) the conduction mechanism through samples with ta-C thickness in the range of 4–30 nm relates to monoenergetic shallow-trap presence in the band gap; (iii) ta-C thickness decrease from 30 to 4 nm leads to the appearance of shallower traps, the decrease of occupation level θ, the increase of their concentration N_t, as well as equilibrium concentration of free charge carriers (n_0); (iv) the sample with 7-nm thick ta-C is characterized by the highest mobility of free charge carriers; and (v) a decrease of ta-C thickness less than 4 nm causes a change of conduction mechanism to SCL current with exponentially distributed traps. The obtained data are in accordance with mobility band-gap measurement results, demonstrating that the band gap value reduces with the ta-C thickness decrease to 7 nm, but further decrease of ta-C thickness leads to a widening of the band gap.

We suppose that the above mentioned dependencies, in the case of the samples with ta-C layer thickness in the range of 2–4 nm, are most likely connected to the formation of a titanium oxide layer at the Ti/ta-C interface as has been suggested earlier. We argue that the ultrathin ta-C layer has nonuniform coverage. In fact, it was demonstrated [45, 46] by means of EELS analysis that both interlayers of Si/Ti and Ti/ta-C contain oxygen as a trace element. Furthermore, the slope values between 3 to 6 are typical to oxide layers [70].

3.3. Influence of quality of underlying titanium layer

In order to confirm the suggestion about a possibility of titanium oxidation, we studied the influence of underlying Ti layer quality by comparing of two samples, which consisted of 20 nm thick as-deposited Ti layer and Ti layer with air-formed native oxide; and 7 nm ta-C on top. In the first case, Ti and ta-C were obtained in one deposition process. In the second case, as-deposited Ti layer was sustained during one week at ambient air to form native surface oxide layer [71, 72].

STM measurements, conductive AFM and current-voltage spectroscopy were carried out with both samples. The presence of native air-formed titanium oxide at the Ti/ta-C interface leads to:

1. A broadening of the band gap value from 1.19±0.2 and 1.92±0.1 eV (measured at ambient air). Thus, we confirm that DOS of underlying layer can influence on the resulting STM spectra.

2. A dramatic drop of the average current J_{SR} from 18.8 to 0.35 nA (measured under 2 V of applied voltage) and a sharp increase of the specific resistance from 200 to $3.22 \cdot 10^4$ Ω cm. Figure 6 demonstrates comparison of topography maps and maps of the current J_{SR}.

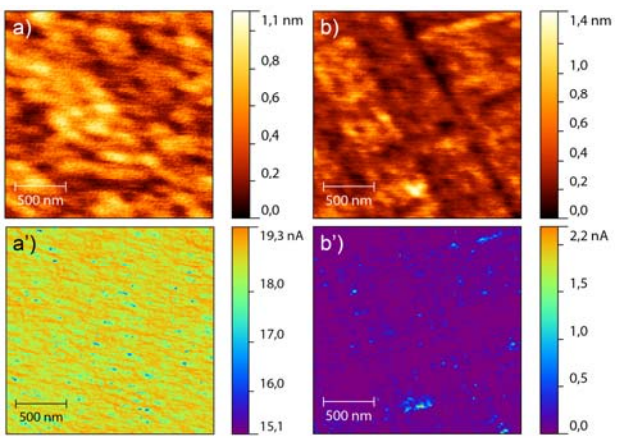

Figure 6. (a–b) Topography maps, (a'–b') maps of current J_{SR} for samples without (a, a') and with (b, b') air-formed native oxide at Ti/ta-C interface (under 2 V).

3. Change of conduction mechanism from SCLC with monoenergetic traps to SCLC with exponentially distributed traps. In a contrast with the current-voltage curve for the sample without native titanium oxide layer at the Ti/ta-C interface (called '7 nm' in Figure 5), the J_{SR}–U_{SR} for the sample with native oxide layer (called '7 nm & ox') does not have signified or separated regions with different slopes. The largest linear region has the slope value N equalled to 3.

4. A decrease of mobility of free charge carriers (Table 1, comparison of '7 nm & ox' and '7 nm').

The same tendency of physical properties change was observed with decrease of ta-C thickness from 4 to 2 nm. Therefore, we suggested that titanium oxide layer can form at the Ti/ta-C interface.

3.4. Band gap calculations

In order to rationalize the obtained experimental results, detailed atomistic simulations were carried out. The resultant JDOS for the samples studied is presented in Figure 7 where the HSE result is compared to that of the same sample obtained with the PBE functional method originally employed in Ref. [51].

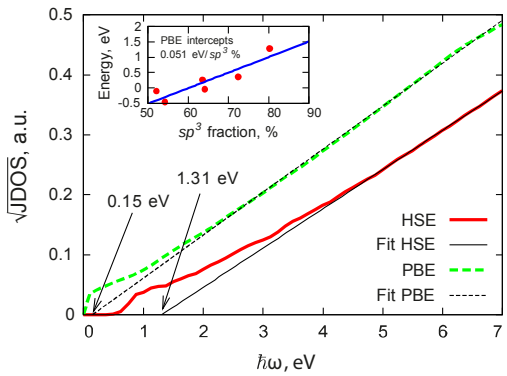

Figure 7. Square root of the JDOS as a function of photon energy for ta-C systems with 72.4 % sp^3 fraction. The straight lines and corresponding numbers give the intercept of first order fits to the linear absorption regime.

The linear fit beyond $\hbar\omega$ = 4.5 eV indicates that the Tauc gap at this sp^3 fraction lies at around 1.3 eV. The PBE calculation severely underestimates this value. It is however much cheaper to carry out PBE calculations, and this allows for the establishment of a trend for the evolution of the Tauc gap as a function of sp^3 fraction, as displayed in the inset of Figure 7. The fitting reveals a linear increase in the Tauc gap of approximately 50 meV per sp^3 percent increase. It should be noted that the suitability of the Tauc approach is limited to high sp^3 fractions; for low densities the states in the pseudogap region of amorphous carbon tend to delocalize. However, the trend clearly points towards a decrease in the band gap value as the amount of sp^2 bonded atoms increases. Since the amount of sp^2 sites is significantly higher in the uppermost 1–3 nm of the experimental structures due to surface reconstruction, this indicates a possible coexistence of a "surface gap" with a "bulk gap". This should result in distinct changes in the electronic properties of the ta-C films as a function of thickness as the relative amount of "surface phase" is changed. Thus, the data obtained from the simulations agree with experimental results.

The band gap prediction shown in Figure 7 is also consistent with the Raman results that indicated that the band gap narrows with decreased ta-C thickness. Simulation results cannot predict that the band gap value starts again to increase when the film thickness is further reduced because the possible titanium oxide layer formation was not taken into account during calculation.

3.5 Electrochemical behaviour

Electrochemical properties of the ta-C thin film electrodes were studied with cyclic voltammetry. First, measurements with cycling speeds of 50 and 400 mV/s was carried out to determine water window and apparent double layer capacitance. A current threshold of 200 µA was used as the limit.

Figure 8 shows the cyclic voltammograms for the bare Ti layer (20 nm) as well as for the electrodes with various thicknesses of top ta-C layer (from 2 to 30 nm) measured at 400 mV/s cycling speed. One can see that potential window measured on electrodes with 7–30 nm top ta-C layer is much wider in comparison to electrodes with 2–4 nm top ta-C, whereas the background current is lower. In addition, the shape of cyclic voltammograms for electrodes with the thinnest ta-C (2–4 nm) replicates the shape of cyclic voltammograms for a bare Ti layer. Therefore, we argue that oxidization and reduction reactions of titanium takes places during cycling.

In the case of electrodes with 7–30 nm thickness of top ta-C, oxidization or reduction of the Ti underlayer was not observed (Figure 8). These samples were stable and show a wide water window as well as reasonably low apparent double layer capacitance (Table 2). Capacitance values were calculated at –1, 0, and +1 V and with cycling speeds of 50 and 400 mV/s. The geometric area of the electrode was used in the calculations and the difference between the anodic and cathodic current densities was used ($\Delta i = 2 \times C \times \upsilon$). As there was hardly any real flat double layer region in the measured voltammograms, it is highly probable that, in addition to pure charging currents, also faradic reactions occur at the electrode surface, which contribute to the calculated double layer capacitance value. Therefore, the double layer capacitances are referred to as pseudocapacitances.

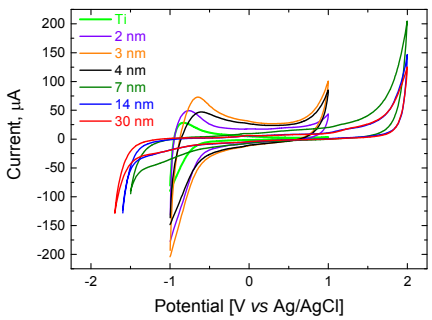

Figure 8. Potential windows for bare Ti layer (20 nm) and electrodes with different thicknesses of top ta-C layers (2–30 nm) in sulphuric acid measured at 400mV/s cycling speed.

Table 2. Potential window and calculated pseudocapacitance values.

ta-C thickness, nm	Potential window ΔE_{sweep}, V	Capacitance, µF/cm^2
7	3.5	145±39
14	3.6	94±37
30	3.7	78±20

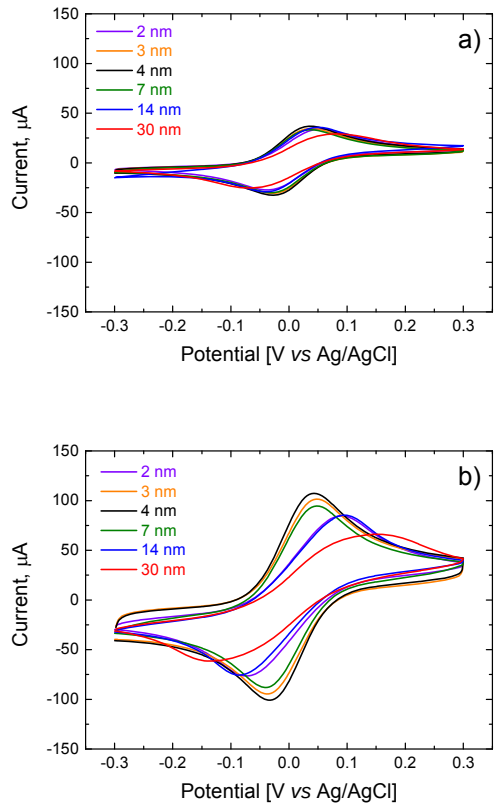

Figure 9. Cyclinc voltammograms of different electrodes with various ta-C thicknesses at cycling speeds of (a) 50 and (b) 400 mV/s.

Table 3. Separation of FcMeOH oxidation and reduction peak potential, oxidation and reduction peak current ratio at cycling speeds for with different ta-C top layer thickness.

ta-C thickness, nm	ΔE_p (FcMeOH), mV	Ip_A/Ip_C	ΔE_p (FcMeOH), mV	Ip_A/Ip_C
	50 mV/s		400 mV/s	
2	91.6 ± 26.7	1.01 ± 0.01	128.3 ± 18.8	1.02 ± 0.01
3	62.4 ± 1.5	1.03 ± 0.01	71.2 ± 2.6	1.04 ± 0.01
4	61.9 ± 0.9	1.02 ± 0.01	69.8 ± 1.5	1.03 ± 0.01
7	60.6 ± 1.0	1.01 ± 0.01	69.9 ± 7.0	1.03 ± 0.01
14	75.7 ± 4.0	0.94 ± 0.01	124.4 ± 29.5	1.02 ± 0.01
30	147.7 ± 0.9	1.01 ± 0.01	282.7 ± 3.4	1.06 ± 0.04

The ferrocene redox couple was used to determine the electron transfer properties of the electrodes as a function of ta-C thickness. The ferrocene redox couple is known to be an outer-sphere redox system (it stays at the outer Helmholtz plane), and is therefore mostly insensitive to electrocatalytic or adsorption steps [3]. In a system with reversible electron transfer, the peak separation ΔE_p is 59 mV regardless of the applied sweep rate. In addition, the ratio of the anodic and cathodic current peaks Ip_A/Ip_C should not deviate markedly from unity. However, as the uncompensated resistance of the electrodes can cause the peaks to shift and the ΔEp to grow irrespective of the electron transfer kinetics. IR compensation with 80 % of the uncompensated resistance was applied. All electrodes were measured three times with both cycling speeds of 50 and 400 mV/s.

The FcMeOH cyclic voltammograms and results of their analysis are shown in Figure 9 and Table 3 for both cycling speeds. It can be seen that electrodes with ta-C thickness in the range of 3 to 7 nm show the lowest ΔE_p, which was close to 61 mV and 70 mV (within the error limits) when cycling speeds were 50 and 400 mV/s, respectively. It should be noted that the ΔE_p values increase as the sweep rate is changed from 50 to 400 mV/s. The peak current ratio is very close to unity for all electrodes with both cycling speeds. The observed behaviour of all the electrodes can be quantified as quasi-reversible with a variable values of heterogeneous transfer coefficient, the latter being highest for the electrodes with ta-C thickness in the range of 3 to 7 nm.

Therefore, decrease of ta-C thickness from 30 to 4 nm leads to the apparently faster electron transfer, which determined by the ferrocene redox couple. This agrees well with the atomistic simulations and scanning tunnelling spectroscopy and conductive-AFM results. It should be recalled that atomistic simulations predicted that the band gap should diminish as the sp^2 fraction increases (essentially as the films become thinner). Experimental study demonstrated that this is satisfied until a certain ta-C thickness (less than 7 nm), when ta-C has nonuniform coverage. Appearance of a titanium oxide layer near the Ti/ta-C interface causes a widening of the band gap and a decrease of conductivity. The possibility of Ti oxidation was demonstrated by means of cyclic voltammetry as well. It was rationalized to be caused by the excessive oxidation of the Ti layer underneath the ta-C thin-film electrodes. Even though there appears to be a relation between the reported changes in the electronic and electrochemical properties for the ta-C thin films, the detailed correlation requires more extensive studies.

4. Conclusions

By utilizing the combination of detailed atomistic simulations and experimental measurements, we can show that in the ideal case of ultrathin ta-C layers, (i) the sp^3/sp^2 ratio will decrease with a decrease in thickness, which leads to (ii) a narrowing of the band gap; (iii) the increase in the current flowing through the thin-film layered structure; (iv) the presence of shallower monoenergetic traps and the increase of their concentration; and (v) the increase of equilibrium concentration of free charge carriers and their mobility. However, in reality, characteristics of the underlying Ti layer and, especially, the possibility of titanium oxide layer formation influence the electronic properties of the entire layered structure in the opposite way. Therefore, several special features associated with the certain ta-C thickness value of 4–7 nm were found. Firstly, there exists the narrowest band gap, the smallest resistivity (maximum of conductivity), the shallowest monoenergetic traps, and the maximum mobility of free chargers. Secondly, the conduction mechanism is shown to change from space-charge-limited current defined by monoenergetic traps to SCL current determined by the presence

of traps with exponentially distributed energy for ta-C thickness less than 7 nm. Such behaviour appears to be (a) due to the formation of a titanium oxide layer at the Ti/ta-C interface and (b) the increase of sp^2 fraction with the thickness decrease. The formation of the titanium oxide layer was observed during the potential window determination with cyclic voltammetry with the samples with ta-C layers thinner than 7 nm, as processes related to Ti oxidation and reduction were seen in the corresponding voltammograms. Based on the electrochemical measurements with the FcMeOH outer sphere redox system, the ta-C electrodes with film thickness between 3–7 nm had the most facile apparent electron transfer kinetics. This was found to be consistent with the experimental and theoretical predictions of the electronic properties of the ta-C films as a function of their thickness. However, further extensive experiments and simulations are needed to explore the behaviour observed here in more detail. Nevertheless, we have demonstrated that electrodes based on ultrathin undoped ta-C can be an alternatives to nitrogen-doped DLC electrodes.

Acknowledgements

The authors would like to acknowledge the Finnish Funding Agency for Technology and Innovation (HILE project, grant number 211488), Academy of Finland together with the National Research Foundation of Korea (CARIBIO project, grant number 132650821), and Aalto University for the financial and technical support. V. P. acknowledges Micronova Nanofabrication Centre and Department of Forest Products Technology for the provision of facilities and technical support; Prof. M.V. Mishin for thorough discussion; Dr. S. Rhode and Prof. M. Moram for TEM imaging; Dr. S. Sintonen for XRR measurements. M.A.C. acknowledges computational resources provided by Aalto University's Science-IT project and CSC IT Center for Science.

Notes

*Corresponding author. vera.protopopova@aalto.fi, vsprotopopova@gmail.com.

[1]Dept. of Materials Science and Engineering, School of Chemical Technology, Aalto University, P.O.Box 16200, FI-00076 Aalto, Espoo, Finland

[2]Dept. of Electrical Engineering and Automation, School of Electrical Engineering, Aalto University, P.O.Box 15500, FI-00076 Aalto, Espoo, Finland

[3]COMP Centre of Excellence in Computational Nanoscience, Department of Applied Physics, Aalto University, P.O. Box 11100, FI-00076 Aalto, Espoo, Finland

[4]Department of Physical Electronics, Saint Petersburg State Polytechnical University, 195251, Polytechnicheskaya st. 29, Saint Petersburg, Russia

References

1. J.-M. Beaulieu, R. R. Gainetdinov, Pharmacol. Rev., 2011, **63(1)**, 182–217.
2. M. D. Hawley, S. V. Tatawawadi, S. Piekarski, R. N. Adams, J. Am. Chem. Soc., 1967, **89(2)**, 447–450.
3. R. L. McGreery, Chem. Rev. 2008, **108**, 2646–2687.
4. L. G. Shaidarova, G. K. Budnikov, Journal of Analytical Chemistry, 2008, **63(10)** 922–942.
5. H. Gerischer, Electrochim. Acta, 1990, **35 (11/12)**, 1677–1999.
6. V. A. Myamlin, Yu. V Pleskov, Russ Chem Rev, 1963, **32 (4)**, 207–223.
7. V. M. Arutyunyan, Sov. Phys. Usp., 1989, **32**, 521–542.
8. Q. Hao, P. Wang, X. Ma, M. Su, J. Lei, H. Ju, Electrochem. Commun., 2012, **21**, 39–41.
9. A. N. Patel, S.-Y. Tan, T. S. Miller, J. V. Macpherson, P. R. Unwin, Anal. Chem., 2013, **85 (24)**, 11755–11764.
10. E. Kaivosoja, S. Sainio, J. Lyytinen, T. Palomäki, T. Laurila, S. Kim, J. Han, J. Koskinen, Surf. Coat. Technol., 2014, **259**, 33–38.
11. E. Kaivosoja, E. Berg, A. Rautiainen, T. Palomäki, J. Koskinen, M. Paulasto-Kröckel, T. Laurila, Conference Proceedings IEEE Eng Med Biol Soc., 2013, 632–634.
12. M. C. Granger, M. Witek, J. Xu, J. Wang, M. Hupert, A. Hanks, M. D. Koppang, J. E. Butler, G. Lucazeau, M. Mermoux, J. W. Strojek, G. M. Swain, Anal. Chem., 2000, **72**, 3793–3804.
13. J. H. T. Luong, K. B. Male, J. D. Glennon, Analyst, 2009,134, 1965–1979.
14. P. U. Arumugam, H. Zeng, S. Siddiqui, D. P. Covey, J. A. Carlisle, P. A. Garris, Appl. Phys. Lett., 2013, **102**, 253107-1–5.
15. A. Fujishima, T. N. Rao, E. Popa, B.V. Sarada, I. Yagi, D.A. Tryk, J. Electroanal. Chem., 1999, **473**, 179–185
16. D. Sopchak, B. Miller, R. Kalish, Y. Avyigal, X. Shi, Electroanalysis, 2002, **14(7–8)**, 473–478.
17. A. Zeng, V.F. Neto, J.J. Gracio, Q. H. Fan, Diamond Relat. Mater., 2014, **43**, 12–22.
18. R. A. Medeiros, A. Benchick, R. C. Rocha-Filho, O. Fatibello-Filho, B. Saidani, C. Debiemme-Chouvy, C. Deslouis, Electrochem. Com., 2012, **24**, 61–64.
19. Y. Tanaka, M. Furuta, K. Kuriyama, R. Kuwabara, Y. Katsuki, T. Kondo, et al., Electrochim. Acta, 2011, **56**, 1172–1181.
20. G. M. Pharr, D. L. Callahan, S. D. McAdams, T. Y. Tsui, S. Anders, A. Anders, et al., Appl. Phys. Lett., 1996, **68**, 779–781.
21. E. Liu, X. Shi, H.S. Tan, L.K. Cheah, Z. Sun, B.K. Tay, J.R. Shi, Surf. Coat. Technol., 1999, **120–121**, 601–606.
22. J. Robertson, Mater. Sci. Eng. R, 2002, **37**, 129–281.
23. H. Cachet, C. Deslouis, M. Chouiki, B. Saidani, N. M. J. Conway, C. Godet, J. Electrochem. Soc., 2002,**149 (7)**, E233–E241.
24. N. Soin, S.S. Roy, S.C. Ray, P. Lemoine, Md.A. Rahman, P.D. Maguire, et al., Thin Solid Films, 2012, **520**, 2909–2915.
25. M. G. Beghi, A. C. Ferrari, K. B. K. Teo, J. Robertson, C. E. Bottani, A. Libassi, and B. K. Tanner, Appl. Phys. Lett., 2002, **81**, 3804–3806.
26. R. McCann, S. S. Roy, P. Papakonstantinou, G. Abbas, J. A. McLaughlin, Diamond Relat. Mater., 2005, **14**, 983–988.
27. I. Rusman, L. Klibanov, L. Burstein, Yu. Rosenberg, V. Weinstein, E. Ben-Jacob, et al., Thin Solid Films, 1996, **287**, 36–44.
28. C. Arena, B. Kleinsorge, J. Robertson, W.I. Milne, M.E. Welland, Diamond Relat. Mater., 1999, *8*, 435–439.
29. B. Marchon, M. Salmeron, Phys. Rev. B, 1989, **39(17)**, 12907–12910.

30. Z. Klusek, Z. Weqar, W. Kozlowski, P. Kowalczyk, E. Denisov, I. Makarenko, et al., Appl. Surf. Sci., 2002, **187**, 28–36.
31. E. Staryga, G.W. Bak, Diamond Relat. Mater., 2005, **14**, 23–34.
32. P.W. May, M.-T. Kuo, M.N.R. Ashfold, Diamond Relat. Mater., 1999, **8**, 1490–1495.
33. E. Liu , X. Shi, L.K. Cheah, Y.H. Hu, H.S. Tan, J.R. Shi, et al., Solid-State Electronics, 1999, **43**, 427–434.
34. L. Klibanov, M. Qksman, A. Seidman, N. Croitoru, Diamond Relat. Mater., 1997, **6**, 1152–1156.
35. N. Koenigsfeld, H. Hofsäss, D. Schwen, A. Weidinger, C. Trautmann, R. Kalish, Diamond Relat. Mater., 2003, **12 (3–7)**, 469–473.
36. A.C. Ferrari, J. Robertson, Phil. Trans. R. Soc. Lond. A, 2004, **362**, 2477–2512.
37. A.C. Ferrari, J. Robertson, Phys. Rev. B, 2000, **61(20)**, 14 095–14 107.
38. G. Irmer, A. Dorner-Reisel, Adv. Eng. Mater., 2005, **7(8)**, 694–705.
39. M.A. Lampert, P. Mark, Current currents in solids, New York and London, Academic press, 1970, 351pp.
40. A. A. Bunakov, A. N. Lachinov, R. B. Salikhov, Technical Physics, 2003, **48 (5)**, 626–630.
41. N. Z. Djalilov, G. M. Damirov, Semiconductors, 2009, **43(11)**, 1521–1525.
42. W. Li, C. Tan, M. A. Lowe, H. D. Abruna, D. C. Ralph, ACS Nano, 2011, **5 (3)**, 2264–2270.
43. P. Hohenberg, W. Kohn, Phys. Rev., 1964, **136**, B864–B871.
44. W. Kohn, L. J. Sham, Phys. Rev., 1965, **140**, A1133–A1138.
45. T. Laurila, A. Rautiainen, S. Sintonen, H. Jiang, E. Kaivosoja, J. Koskinen, Mater. Sci. Eng. C, 2014, **34C**, 446–454.
46. T. Laurila, V. Protopopova, S. Rhode, S. Sainio, T. Palomäki, M. Moram, et al., Diamond Relat. Mater., 2014, **49**, 62–71.47. F.-X. Liu, Z.-L. Wang, Surf. Coat. Tech., 2009, **203**, 1829–1832.
48. J. Tauc, R. Grigorovici, A. Vancu, Phys. Stat. Sol. B, 1966, **15**, 627–637.
49. S. Knief, W. von Niessen, Phys. Rev. B, 1999, **59**, 12940–12946.
50. S. K. O'Leary, S. R. Johnson, P. K. Lim, J. Appl. Phys., 1997, **82**, 3334–3340.
51. M. A. Caro, R. Zoubkoff, O. Lopez-Acevedo, T. Laurila, Carbon, 2014, **77**, 1168–1182.
52. J. P. Perdew, K. Burke, M. Ernzerhof, Phys. Rev. Lett., 1996, **77**, 3865–3868.
53. J. P. Perdew, M. Levy, Phys. Rev. Lett., 1983, **51**, 1884–1887.
54. J. Heyd, G. E. Scuseria, M. Ernzerhof, J. Chem. Phys., 2003, **118**, 8207–8215.
55. M. A. Caro, J. Määttä, O. Lopez-Acevedo, T. Laurila, J. Appl. Phys. , 2015, 117, 034502-1–9.
56. G. Kresse, J. Furthmüller, Phys. Rev. B, 1996, **54**, 11169–11186.
57. P. E. Blöchl, Phys. Rev. B, 1994, **50**, 17953–17979.
58. G. Kresse, D. Joubert, Phys. Rev. B, 1999, **59**, 1758–1775.
59. R. M. Feenstra. Scanning Tunneling Microscopy: Semiconductor Surfaces, Adsorption, and Epitaxy in a book Scanning Tunneling Microscopy and Related Methods, NATO ASI Series, 1990, **184**, 211–240.
60. S. Aljishi, J. D. Cohen, S. Jin, L. Ley Phys. Rev. Lett., 1990, **64**, 2811–2814.
61. V. I. Ivanov-Omskii, A. V. Tolmatchev, S. G. Yastrebov, Semiconductors, 2001, **35(2)**, 220–225.
62. K.-F. Lin, H.-M. Cheng, H.-C. Hsu, L.-J. Lin, W.-F. Hsieh, Chem. Phys. Lett., 2005, **409**, 208–211.
63. M. S. Selim, M. E. Gouda, M. G. El-Shaarawy, A. M. Salem, W. A. Abd El-Ghany, Thin Solid Films, 2013, **527**, 164–169
64. R. Rajalakshmi, S. Angappane, J. Alloys Compd., 2014, **615**, 355–362.
65. E. S. M. Goh, T. P. Chen, C. Q. Sun, Y. C. Liu, J. Appl. Phys., 2010, **107**, 024305-1–5.
66. N. E. Makori, I. A. Amatalo, P. M. Karimi, W. K. Njoroge, American Journal of Condensed Matter Physics, 2014, **4(5)**, 87–90.
67. A. A. Mulama, J. M. Mwabora, A. O. Oduor, C. M. Muiva, C. M. Walloga, IOSR-JAP, 2014, **6(5)**, 1–6.
68. R. M. Feenstra, J. A. Stroscio, J. Vac. Sci. Technol. B, 1987, **5**, 923–929.
69. D.-Z. Guo, S.-M. Hou, G.-M. Zhang, Z.-Q. Xue, Appl. Surf. Sci., 2006, **252**, 5149–5157.
70. T. Harada, I. Ohkubo, K. Tsubouchi, H. Kumigashira, T. Ohnishi, M. Lippmaa, et al., Appl. Phys. Lett., 2008, **92**, 222113-1–3.
71. V. A. Matveev, N. K. Pleshanov, A. P. Bulkin, V. G. Syromyatnikov, Journal of Physics: Conference Series, 2012, **340**, 012086-1–4.
72. E. McCafferty, J. P. Wightman, Appl. Surf. Sci., **143**, 1999, 92–100.

